Label-Free C-Reactive Protein Si Nanowire FET Sensor Arrays With Super-Nernstian Back-Gate Operation

Luca Capua, *Graduate Student Member, IEEE*, Yann Sprunger, H. Elettro, F. Risch, A. Grammoustianou, R. Midahuen, T. Ernst, *Senior Member, IEEE*, S. Barraud, R. Gill, and A. M. Ionescu, *Fellow, IEEE*

***Abstract*— We present a CMOS-compatible double gate and label-free C-reactive protein (CRP) sensor, based on silicon on insulator (SOI) silicon nanowires arrays. We exploit a reference subtracted detection method and a super-Nernstian internal amplification given by the double gate structure. We overcome the Debye screening of charged CRP proteins in solutions using antibodies fragments as capturing probes, reducing the overall thickness of the capture layer. We demonstrate the internal amplification through the pH response of the sensor, in static and real-time working modes. While operated in back-gate configuration, the sensor shows excellent stability (<20 pA/min in the worst case), low hysteresis (<300 mV), and a great sensitivity up to 1.2 nA/dec toward CRP proteins in the linear response range. The reported system is an excellent candidate for the continuous monitoring of inflammation biomarkers in serum or interstitial fluid.**

***Index Terms*— Biosensors, C-reactive protein (CRP), double-gate FET, protein detection, silicon nanowires (SiNWs), silicon on insulator (SOI).**

I. Introduction

C-REACTIVE protein (CRP) is an acute-phase protein whose concentration significantly increases in case of inflammation. Since its discovery in 1930, CRP was extensively studied and revealed to be a key biomarker with pleiotropic diagnostic applications in immunology, oncology, cardiomyopathy, and other chronic conditions such as renal diseases and type II diabetes. The median CRP level in healthy patients is about 0.8 μg/mL (6.66 nM) and can increase by up to 10 000 fold in the presence of an acute infection.

In the recent context of the global COVID-19 pandemic, CRP levels were closely monitored and appeared well correlated with the severity of the symptoms of patients infected by SARS-CoV-2.

It was shown that the hospitalization-wide median CRP was significantly higher among the patients who died, compared with those who survived. Moreover, patients who survived had lower peak CRP levels and earlier declines [1], [2]. Thus making CRP a highly relevant marker in assessing a patient's conditions together with other clinical findings, such as IL-6 levels and SaO_2 [3]. We believe that a continuous label-free CRP biosensor can reveal to be an instrumental tool for the diagnosis of acute and chronic conditions with potentially life-saving outcomes. Many studies demonstrate that field effect transistors are optimal candidates as the core technology to develop highly sensitive biosensors, thanks to their scalability, possibility of miniaturization, and label-free detection capabilities [4]. Among the different types of devices based on a field-gating effect, silicon nanowires (SiNWs) are the best candidates to achieve high analytical sensitivity and lower limit of detection (LoD) [5]. The CMOS compatibility makes SiNWs ideal for integration in miniaturized wearable and portable systems that require a low power consumption. In precedent works, SiNWs have been used for the detection of proteins, such as cardiac Troponin [6]–[9], prostate cancer risk biomarkers [10]–[12], label-free detection of deoxyribonucleic acid (DNA) [13], viruses [14], cortisol [15], vascular endothelial growth factor (VEGF) molecules [16], and MicroRNA [17]. SiNWs have also been used for the detection of CRP [9], [18], [19], but so far the detected concentration range has been too low with respect to the physiological one in patients with inflammatory diseases. The large number of publications demonstrates the high versatility of SiNWs as biosensors. These devices employ an electrical based detection of the antigens in solution, thanks to a field effect modulation of the conductivity of the nanowires (NWs), controlled by

Manuscript received November 23, 2021; revised January 7, 2022; accepted January 9, 2022. Date of publication February 10, 2022; date of current version March 28, 2022. This work was supported by the European Union's Horizon 2020 Research and Innovation Program under Grant 101017915 (DIGIPREDICT) and Grant 961703 (Cyto-Track). This article is an extended version of a paper presented at IEDM 2021. *(Luca Capua and Yann Sprunger contributed equally to this work.) (Corresponding author: Luca Capua.)*

Luca Capua, F. Risch, and A. M. Ionescu are with the Nanoelectronic Devices Laboratory, Ecole Polytechnique Fédérale de Lausanne (EPFL), 1015 Lausanne, Switzerland (e-mail: luca.capua@epfl.ch; felix.risch@epfl.ch; adrian.ionescu@epfl.ch).

Yann Sprunger is with the Nanoelectronic Devices Laboratory, Ecole Polytechnique Fédérale de Lausanne (EPFL), 1015 Lausanne, Switzerland, and also with Xsensio SA, 1015 Lausanne, Switzerland (e-mail: yann.sprunger@xsensio.com).

H. Elettro, A. Grammoustianou, and R. Gill are with Xsensio SA, 1015 Lausanne, Switzerland (e-mail: herve.elettro@xsensio.com; aristea.grammoustianou@xsensio.com; ron.gill@xsensio.com).

R. Midahuen, T. Ernst, and S. Barraud are with CEA, LETI, Nanotechnology Department, Université Grenoble Alpes, 38000 Grenoble, France (e-mail: rony.midahuen@cea.fr; thomas.ernst@cea.fr; sylvain.barraud@cea.fr).

Color versions of one or more figures in this article are available at https://doi.org/10.1109/TED.2022.3144108.

Digital Object Identifier 10.1109/TED.2022.3144108

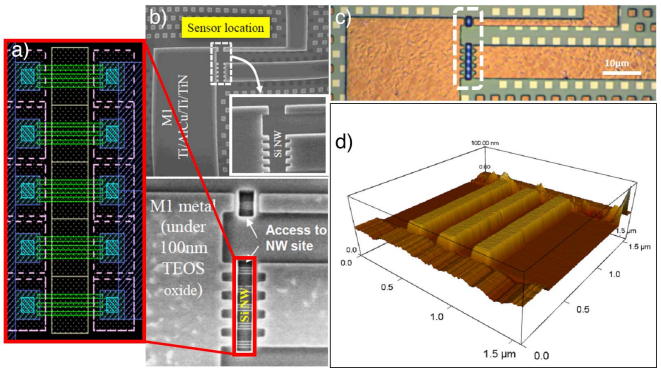

Fig. 1. (a) Details of the layout of a SiNWs array on the bio-FET chip. The sensor is made by 15 parallel identical NWs. (b) SEM images with details of the SiNWs and metallic lines, provided by CEA LETI. (c) Optical microscope image highlighting the opening of the passivation to reach the SiNWs. (d) AFM image showing the details of three parallel SiNWs. The width of each NW is confirmed to be 150 nm.

the presence of charged molecules in the liquid-gate terminal. Compared with classical MOSFET used as the core of biosensing systems, SiNWs offer a larger surface-to-volume ratio, and they are more sensitive to surface charge modulation. In this work, we propose a CRP biosensor based on a SiNWs array field effect transistor. The array is formed by 15 identical NWs, with a width of 150 nm and a length of 1 μm. The larger area offered by the NWs array allows to have a higher number of binding sites for the analyte. Thus, we increase the detectable concentration range, allowing monitoring of CRP in the relevant levels for human biofluids. Moreover, we propose a double gate configuration, which enhances the sensor response, thanks to internal amplification. In addition, common mode drift and unspecific binding response are removed thanks to a reference subtracted operation mode.

II. SiNWs Array Fabrication

The fabrication process flow has been entirely developed at CEA LETI. In our International Electron Devices Meeting (IEDM) 2021 paper (Capua and Sprunger, *et al.*), we presented the main steps of the process flow used for the fabrication of SiNWs sensors based on multiwire of 150 nm width and 1 μm length. The Si layer is thinned down to 30 nm, followed by the patterning of the SiNWs arrays by photolithography (a combination of *e*-beam and deep ultraviolet (DUV) lithography), followed by a reactive ion etching step to remove the excess of Si. After the creation of the source–drain contacts by ion implantation, thermal oxidation was used to grow 2.5 nm of silicon dioxide, followed by a deposition of 2 nm of high-k dielectric (HfO_2). A SiN passivation layer was deposited, prior to contact and metal lines scheme definition. Finally, The SiNWs test sites are accessed through the passivation layer by an etching step. Fig. 1(a) shows the layout of the NWs array. In Fig. 1(b), two SEM images show the access through the passivation layer, with at the bottom of the trench the 15 SiNWs composing the array. Fig. 1(c) shows the same details with an optical microscopy image. Fig. 1(d) shows a triplet of NWs through AFM analysis.

III. Materials and Methods

A. Chemicals and Surface Functionalization

All reagents and solvents were used as received without further purification. BR228-D4A3 CRP recombinant monoclonal antibody fragments (Fab) were purchased from *BBI Solutions*, (3-aminopropyl) triethoxysilane (APTES), and di(n-succinimidyl) glutarate (DSG) was purchased from *Sigma Aldrich*. StartingBlock[1] blocking buffer was purchased from *ThermoFisher Scientific*.

B. Surface Characterization–X-Ray Photoelectron Spectroscopy

X-ray photoelectron spectroscopy (XPS) measurements were carried out using a PHI VersaProbe II scanning XPS microprobe (Physical Instruments AG, Germany).

Analysis was performed using a monochromatic Al Kα X-ray source of 24.8 W power with a beam size of 100 μm. The spherical capacitor analyzer was set at 45° take-off angle with respect to the sample surface. The pass energy was 46.95 eV, yielding a full width at half maximum of 0.91 eV for the Ag 3d 5/2 peak. Curve fitting was performed using the PHI Multipak software.

C. Electrical Characterization

All the measurements have been performed at room temperature and standard laboratory conditions. A Keithley 4200A-SCS Parameter Analyzer from Tektronix© was used to perform the reported electrical characterization.

D. Surface Plasmon Resonance

To perform surface plasmon resonance (SPR) measurements, a Biacore 8K high-throughput and high-sensitivity SPR system has been employed. CRP Free Serum was purchased from HyTest (Cat. #8CFS); EDC (1-ethyl-3-(3-dimethylaminopropyl)carbodiimide hydrochloride) and NHS (N-hydroxysuccinimide), MES (2-(N-morpholino) ethanesulfonic acid) buffer, 11-mercaptoundecanoic acid (MUA), and ethanolamine were purchased from Fisher Scientific. HBS-P assay diluent buffer was prepared using 0.01M HEPES (4-(2-hydroxyethyl)-1-piperazineethanesulfonic acid) pH 7.4, 0.15M NaCl, and 0.005% v/v surfactant P20 purchased from Sigma Aldrich.

IV. Electrical Characterization

Before using the SiNW arrays as biosensors, a full electrical characterization to assess the NWs-FET performances has been carried out. The gate voltage is applied through an external standard Ag/AgCl reference electrode (from MicruX Technologies) immersed in the liquid solution in contact with the gate of the SiNW arrays, as shown in Fig. 2(a). Fig. 2(b) shows the transfer characteristic of one SiNW array biased with different back-gate voltages, $V_S = 0$ V and $V_D = 0.3$ V. The sensor shows to be easily and reliably tunable, in order to position the bias point in the desired working region: by tuning the back-gate voltage, it is possible to

[1]Trademarked.

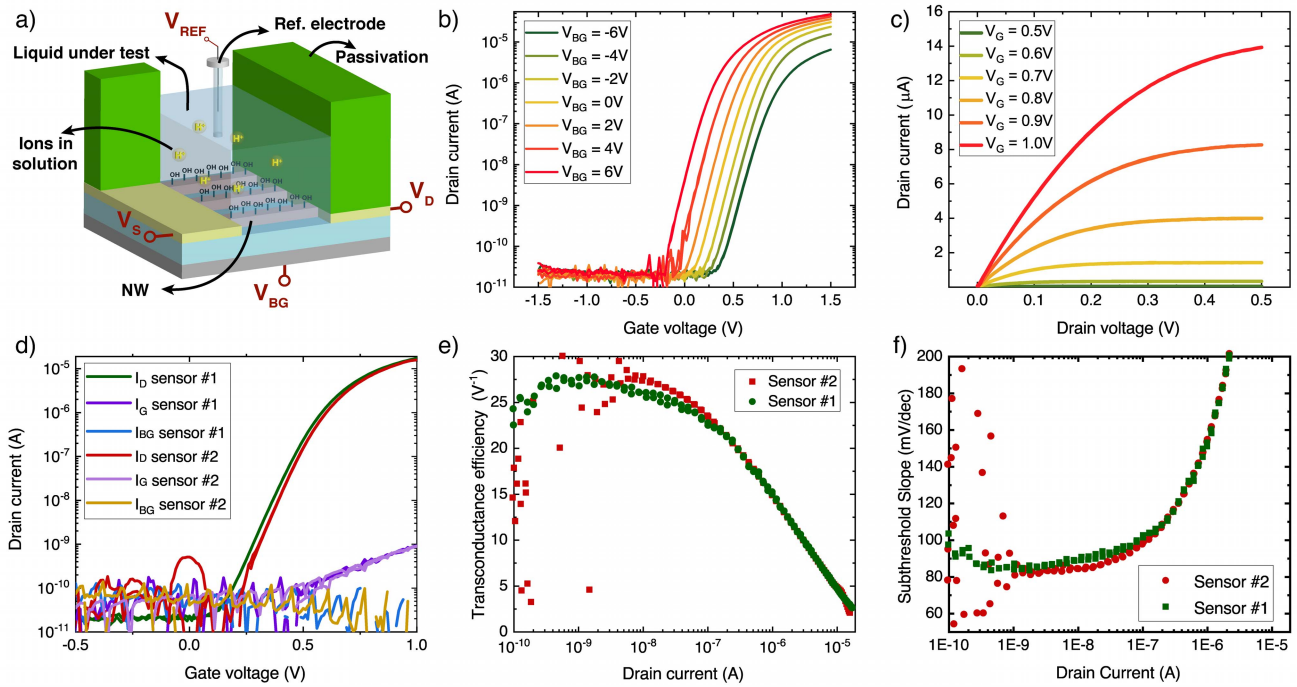

Fig. 2. (a) Setup schematic. The sensor is a four terminals device, with a drain, a source, a back gate, and an external Ag/AgCl electrode in solution as gate terminal. The gate voltage is modulated through the reference electrode immerged in liquid. (b) Tunable transfer (I_D–V_G) characteristic by applying different back-gate voltages. (c) Output I_D–V_D characteristic for different applied V_G and $V_{BG} = 0$ V. (d) I_D–V_G for two SiNW arrays. In the same graph, the leakage currents (gate, I_G and back-gate, I_{BG}) for are reported both devices. The applied back-gate voltage is $V_{BG} = 0$ V. (e) Transconductance efficiency for the two measured sensors. (f) SSs as a function of the drain current.

work in subthreshold regime with a $V_{GS} = 0$ V. The output characteristic, I_D–V_D, of one sensor is shown in Fig. 2(c) for different applied gate voltages. The double-sweep transfer characteristic of two arrays (called here sensor #1 and sensor #2) is shown in Fig. 2(d), while the source (V_S) and back-gate (V_{BG}) voltages are kept constant at 0 V, and the drain voltage (V_D) is 0.3 V. In the same plot, the two leakage currents are reported (gate and back-gate leakages) for each array. The two SiNW FETs show an ON–OFF-ratio of 10^6, low hysteresis, and similar response. In Fig. 2(e), we report the ratio between the transconductance, $g_m = \partial I_D/\partial V_G$, and the drain current, a parameter known as transconductance efficiency. In traditional FETs at room temperature, the maximum transconductance efficiency is physically limited to 38.5 V^{-1} [20]. In our case, the performances are comparable with those found in literature [21], [22] and with standard bulk Si-FET [23], [24], reaching peaks of 30 V^{-1} in weak inversion working regime. The transconductance efficiency is a key parameter for analog application and design [25], but it was also proven to be an important feature for the design and development of biosensors [26]. The sensitivity of a sensor in weak inversion region can be related to the subthreshold slope (SS $= \partial V_G/\partial(\log_{10}(I_D))$) of the transistor. A steep characteristic is fundamental to achieve high sensitivity and to increase the sensor resolution. In Fig. 2(f), we report the values of the SS of our sensors, comparable with the best devices in literature.

V. pH Sensing

The SiNW arrays are four-terminal devices, with common source contacts, an independent drain, a back-gate, and a liquid gate contact. Thanks to the double-gate structure, the sensor can be used either in top gate (TG, V_{BG} set constant, and $V_G = V_{REF}$ swept through an external Ag/AgCl reference electrode) or bottom gate (BG, V_{REF} set constant, and V_{BG} swept through the Si back-gate contact) configuration. We used static and continuous pH measurement to prove the capability of the SiNWs to work as liquid-gated sensors and to assess the ability to overcome the Nernst limit of 59 mV/pH. Before testing the SiNW arrays as pH sensor, a polydimethylsiloxane (PDMS) stamp was placed on top of the chip, to confine the liquid under test over the NWs and to define a constant volume of the liquid. The pristine chip, with the HfO_2 layer exposed to the liquid under test, has been tested toward different pH solutions (phosphate buffer solutions). As already known, SiNWs with high-k dielectric are an optimal substrate for pH detection [27], [28]. In Fig. 3(a), we report the I_D–V_G characteristic of one array for different pH values in TG configuration. Fixing an arbitrary drain current, and extracting the corresponding V_{REF} ($=V_G$), we obtain the data points in Fig. 3(b). We can notice that the extracted values follow a linear trend, characterized by a Nernstian pH sensitivity of 60 mV/pH. The sensor operated in TG configuration shows low hysteresis and high repeatability for different injections of the same value of pH. A second experiment was carried out by biasing the FET array in back-gate configuration, with $V_S = V_{REF} = 0$ V, $V_D = 0.3$ V, and V_{BG} swept between 15 and 35 V. The curves show a low hysteresis and a good ON–OFF-ratio of 10^5. The I_D–V_{BG} curves show a right shift for different pH solutions, in accordance with the TG mode experiment. After recording the transfer characteristics I_D–V_{BG} [Fig. 3(c)],

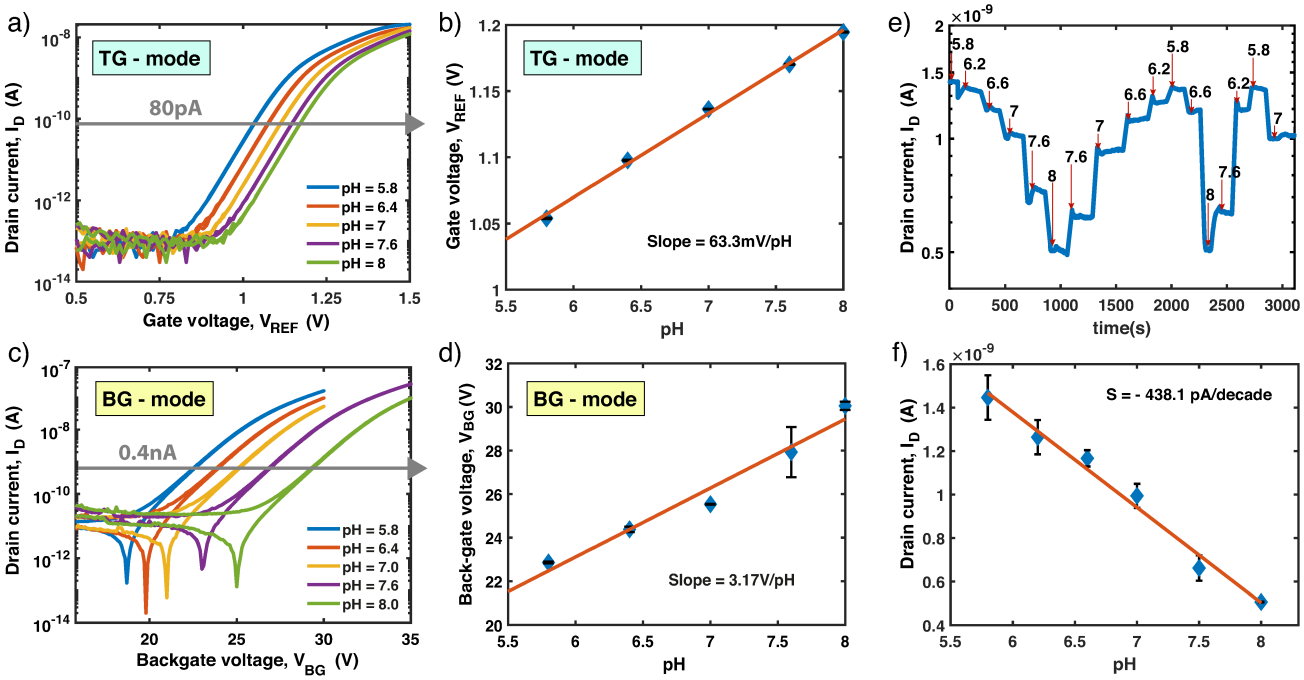

Fig. 3. (a) I_D–V_{REF} curves of the sensor operated in TG mode for different pH values. V_{BG} and V_S were fixed at 0 V, while $V_D = 0.3$ V. The gate voltage V_{REF} was applied through an external Ag/AgCl reference electrode immersed in solution. (b) Extracted values of the reference voltage at a fixed arbitrary current. The linear response shows a sensitivity of 63.3 mV/pH, close to the Nernstian limit. (c) I_D–V_{BG} curves of the sensor operated in BG mode for different pH values. $V_{REF} = V_S = 0$ V, $V_D = 0.3$ V. (d) Extracted values of the back-gate voltage for different pH at a fixed drain current. The linear response shows in back-gate configuration a sensitivity higher than 3 V/pH, demonstrating an internal amplification by a factor of 50. (e) Real-time response to pH variations. The sensor is biased with $V_{BG} = V_S = 0$ V and $V_D = V_{REF} = 0.3$ V. (f) Drain current values extracted from (e), with a linear interpolation.

a value of current in the weak inversion working regime was selected to extract the correspondent V_{BG} values for different pH solutions. As shown in Fig. 3(d), the sensitivity in BG configuration spikes up to more than 3 V/pH, obtaining a 50× internal amplification. The amplification beyond the Nernst limit could be explained by the difference between the top and bottom oxides. In fact, the ratio between the two capacitive couplings can be related to the demonstrated amplification, as already explained in previous modeling studies [29]. In our work, we exploit this internal amplification to target the physiological CRP concentration range (0.5−500 μg/mL), being able to resolve small concentration changes in solution with appropriate analytical sensitivity and no need for sample dilution. We also proved that the system can reliably detect pH changes in solution in real time, as reported in Fig. 3(e) and (f), in phosphate buffers, for a pH range between 5.8 and 8.0, both in increasing and decreasing pH values.

VI. Functionalization

In order to build a specific CRP capture layer, antibody fragments (Fab) were immobilized on the NWs hafnium oxide surface, as described in our IEDM 2021 paper. First, the surface was rinsed with 99% ethanol and carefully dried with N_2. To ensure an effective surface coverage of the hydroxyl-terminated oxide surface, the SiNWs were exposed to plasma oxygen at 30 W for 1 min and immediately incubated in a 2% APTES solution in 95% ethanol for 1 h. After incubation, the chip was rinsed with ethanol and dried with N_2. The SiNWs were subsequently annealed at 120 °C to obtain an ordered monolayer [7]. The APTES-modified surface was immersed in 1-mM DSG crosslinker in an aqueous solution [1X phosphate buffer saline (PBS)] for 10 min, to create an amine-reactive surface. The amine-reactive homo-bifunctional crosslinker was exploited to immobilize the CRP Fab (active channel), as well as the fluorescein isothiocyanate (FITC) Fab (reference channel), by immersing the NWs in 20-μg/mL Fab antibodies diluted in 1X PBS for 1 h. The unbounded antibodies were removed by washing the surface with 1X PBS solution. To avoid unspecific surface binding, the surface was blocked with StartingBlock[1] blocking buffer (*ThermoFisher*), and the unreacted sites were quenched with 1M ethanolamine. To prove the correct surface functionalization, the different steps were assessed by XPS analysis performed on HfO_2 surfaces. A silicon chip with a thermally grown 200-nm layer of SiO_2 was taken as a reference control. The modulation of the C1s peak for the different steps is shown in Fig. 4(a). As expected, after the first step of surface silanization, the carbon peak at 285 eV (C–C) increases in intensity, due to the carbon backbone of the APTES molecules. After linking the antibodies to the surface, a secondary peak at 288.3 eV appears, indicating the formation of the peptide bond (NHC = O), thus the correct attachment of the antibodies to the surface (blue curve). In comparison, the control sample that did not go through the silanization process (green curve) does not show the secondary peak, indicating that the antibodies were not able to correctly attach to the oxide surface.

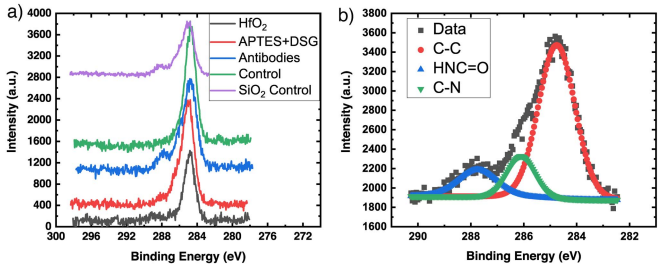

Fig. 4. (a) XPS spectra of different samples at different functionalization steps. The black curve shows the response of the HfO_2 bare surface, where the C–C peak at 285 eV is given by surface contamination. The red curve shows the response of the HfO_2 surface after immersion in APTES and crosslinker (DSG) as described in the functionalization section. The blue curve shows the response of the same chip after antibodies immobilization. A characteristic peak at 288.3 eV indicates the presence of the correctly attached antibodies. Green and purple curves are two control surfaces, respectively, an HfO_2 surface that did not undergo the silanization process prior antibodies attachment, and a SiO_2 reference surface. (b) C1s peak fitting for the HfO_2 functionalized sample with antibodies. The figure shows the formation of a secondary peak at 288.3e V, indicating the correct functionalization with antibodies.

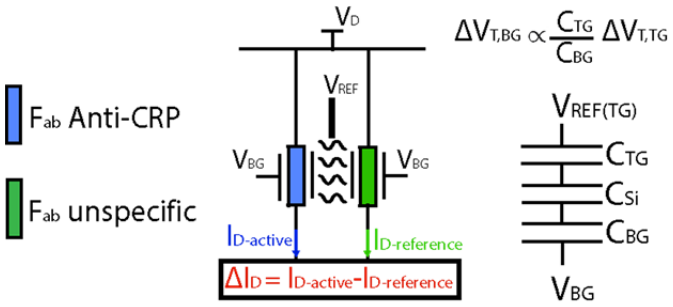

Fig. 5. Reference subtracted response principle: two identical SiNW arrays are functionalized with antibodies fragments specific to CRP, and specific to FITC, respectively. The final signal is obtained by subtracting the output currents of the two devices. Furthermore, we exploit an internal amplification between the TG and the BG voltage shifts at constant current, given by the ratio of the two oxide capacitances.

The control SiO_2 sample (purple curve) shows the same specific secondary peak, confirming that the functionalization works both on a standard silicon dioxide surface and on a high-k dielectric one, such as the HfO_2. Fig. 4(b) shows the detailed fitting of the XPS spectrum of the correctly functionalized HfO_2 sample, with each contribution to the overall signal.

VII. Detection Results

A. Reference Subtracted Configuration

Drift and unspecific response are two of the most challenging problems in biosensors based on field effect transistors. Drift and noise can hide the signal response to analytes, and in many applications, individual sensors calibration is required prior to usage of the sensor. Moreover, the binding of nonspecific analytes can lead to falsely positive unspecific response and, hence, lowers the specificity of the biosensor. In order to remove drift effects and unspecific binding signals from our sensor response, we exploited a reference-subtracted operation mode described in Fig. 5. The latter consists in using two identical SiNWs arrays made of 15 parallel NWs ($W = 150$ nm, $L = 1$ μm) immobilized with anti-CRP (active) and anti-FITC (reference) Fab fragments, respectively. We can obtain the output response by subtracting the output current of the reference sensor from the active one. Thanks to the subtraction of the two signals, the common mode noise and drift are removed, together with the common unspecific response between the two arrays (under the assumption of homoscedasticity and monotonicity of the drift). Both devices can either be operated in TG or BG mode. While operating in the BG one, the charges-induced voltage signal at the TG ($\Delta V_{T,TG}$) is seen as an amplified signal at the BG ($\Delta V_{T,BG}$), with an amplification factor proportional to the ratio of the two capacitive couplings between the liquid gate and the channel (C_{TG}) and the BG and the channel (C_{BG}), as sketched in Fig. 5.

B. Anti-CRP Fab Binding Kinetics

We studied the binding kinetic between the anti-CRP Fab fragments and CRP using SPR technique. For SPR measurements, a bare gold chip was first functionalized overnight with MUA at 1 mM. After extensive wash with ethanol and deionized water (DI), the chip was placed in a Biacore 8K SPR for further immobilization and dose response assessment. The carboxylic group of the MUA is activated using an EDC/NHS activation followed by the injection of 20 μg/mL of the CRP Fab fragment in 10-mM MES buffer at pH 6.0. After antibodies immobilization, the unreacted sites were quenched with 1M ethanolamine. Finally, the sensor was washed for 1 h in assay diluent before being challenged with CRP concentrations ranging from 0.025 to 2.5 μg/mL.

The sensor showed a specific and dose-dependent response, as expected [Fig. 6(a)]. The extracted dissociation constant (Kd) of the CRP Fab fragment–CRP interaction is around 1 μg/mL (8 nM). When challenged with the same concentrations of bovine serum albumin (BSA), the sensor does not show any nonspecific signal. It is highly interesting to observe that after fitting the SiNW response (explained in detail in the next paragraph) with a four parameters logistic regression [30] [Fig. 6(b)], we find a dissociation constant (Kd) for the CRP Fab fragment–CRP interaction of approximately 1.3 μg/mL. This value is in very good agreement with the SPR output.

C. SiNWs Drift and Stability

Before testing the specific response of the sensor to CRP in buffer, we studied the stability of the response to only assay diluent (0.1X PBS). It is fundamental for a sensor to show stability when tested against blank buffers, to ensure that the change in the output current while tested with a specific analyte corresponds to a specific response. Fig. 6(c) shows the I_D–V_{BG} response of the active sensor, for four injections of the same buffer. The curves are characterized by a small hysteresis (<300 mV) in double-sweep measurements, and a negligible shift over time (each measurement is taken every 10 min). In order to quantify the drift in time, five different back-gate voltages have been fixed to extract the correspondent drain current value. This process has been repeated for the responses of the active (functionalized with anti CRP-Fab) and the reference (functionalized with anti FITC-Fab) sensors. The two responses are then subtracted

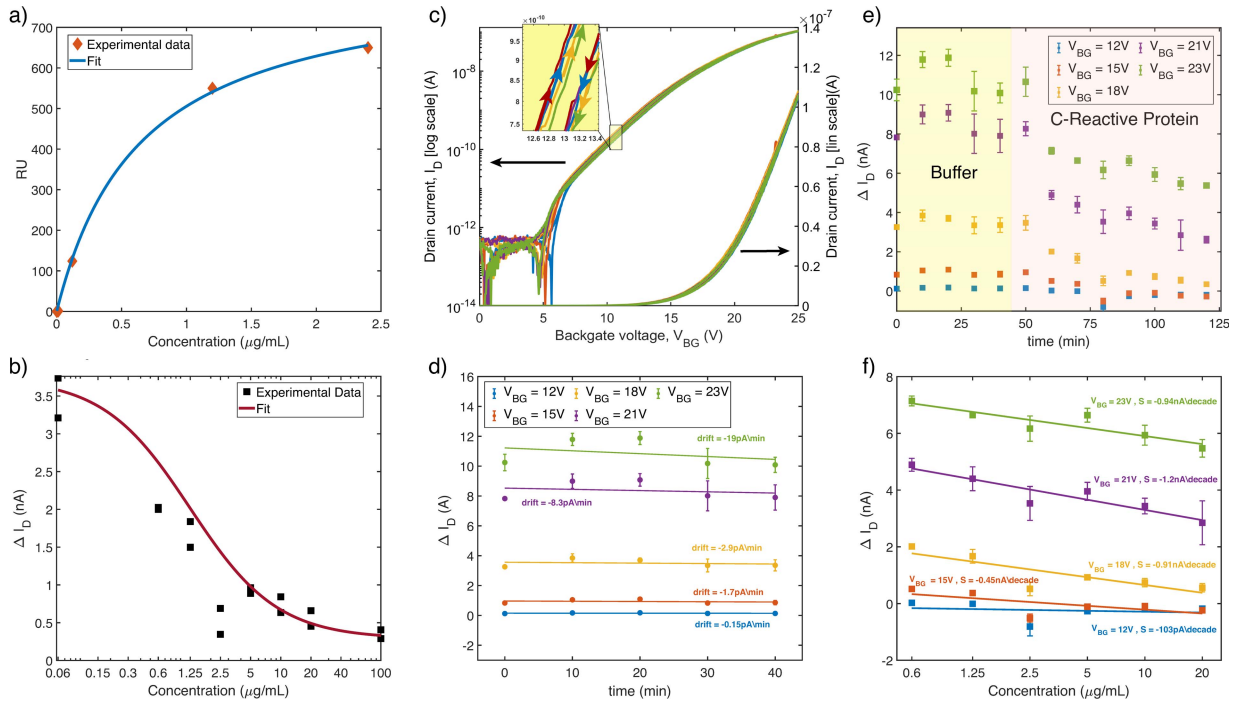

Fig. 6. (a) CRP dose response in SPR: response of Fab anti-CRP fragments to CRP spike-ins in 0.01M HEPES pH 7.4, 0.15M NaCl, and 0.005% v/v Surfactant P20 used both as running buffer and assay diluent. The data are fit with a 4PL regression. (b) SiNW biosensor in back-gate configuration ($V_{REF} = 0$ V, VD-active $=$ VD-reference $= 0.3$ V, $V_{BG} = 18$ V). The response of Fab anti-CRP fragment to CRP spike-ins in 0.01X PBS and 0.1% BSA is fitted with a 4PL regression, showing a Kd of 1.3 μg/mL. The R^2 value obtained by fitting the experimental data is 0.82. (c) I_D–V_{BG} curves of the sensor operated in BG mode for four buffer injections, every 10 min of incubation. $V_{REF} = V_S = 0$ V, $V_D = 0.3$ V. The inset shows a low drift and hysteresis. (d) Differential response of the sensor to buffer injections as a function of time, at different fixed back-gate voltages. The slope of the linear fit indicates the drift over time. (e) Complete differential response over time for different fixed back-gate voltages (incubation time is 10 min per injection). Larger changes in the current are given for higher fixed voltages, together with lower stability during buffer injections. (f) Extracted differential response for different voltages. The slope of the linear fit shows that the sensitivity is higher for higher back-gate voltage.

to obtain $\Delta I_D = I_{D\text{-active}} - I_{D\text{-reference}}$ for different fixed back-gate voltages. These values are reported as a function of time in Fig. 6(d), to visualize the drift over time. In the worst case (at higher back-gate voltage), the drift corresponds to -19 pA/min, and the signal is characterized by a higher noise (standard deviation from the linear fit). For all the regions, the drift over time results in at least 50 times lower than the sensitivity of the sensor to CRP injections.

D. SiNWs CRP Response

To assess the sensitivity against CRP in a physiological range, a differential measurement in back-gate configuration mode has been used, exploiting the intrinsic sensitivity amplification of the double-gate SiNWs system. We biased the active and the reference SiNW sensor arrays with a constant reference voltage $V_{REF} = 0$ V, and $V_{DS\text{-active}} = V_{DS\text{-reference}} = 0.3$ V. Sweeping the common back-gate voltage, we systematically recorded the two sensors' responses, in order to obtain the differential response toward different CRP concentrations in the physiological range between 0.5 and 100 μg/mL, in 0.1X PBS buffer. We report in Fig. 6(e) the complete reference subtracted response $\Delta I_D = I_{D\text{-active}} - I_{D\text{-reference}}$ as a function of time, being the incubation time after each injection equal to 10 min. In the yellow part of the plot, we report the differential response for the blank measurements, i.e., the sensor stability, while in the orange part, we report the response to CRP injections. These results show that there is a tradeoff between sensor stability and sensitivity: at higher fixed back-gate voltages, we obtain a higher response to CRP, but also higher instability for the blank buffer response. The best tradeoff between stability during blank buffer injections and the sensitivity to different CRP concentration injections is obtained for $V_{BG} = 18$ V. We report the linear sensitivity response in the range between 0.6 and 20 μg/mL in Fig. 6(f), for different fixed back-gate voltages. As shown in our IEDM 2021 paper, the active sensor response shows a clear shift for different CRP concentrations. The sensor shows a monotonically decreasing linear response in logarithmic scale, with sensitivities ranging between -103 pA/dec for $V_{BG} = 12$ V and -1.2 nA/dec for $V_{BG} = 21$ V. Moreover, the best analog performances are usually obtained in the weak inversion regime (lower voltages), thus while designing the sensor and the read-out circuit, it is recommended to take into consideration all the involved parameters, such as stability, gain, SS, and transconductance efficiency.

VIII. Conclusion

We successfully fabricated and reported a CRP label-free biosensor based on SiNW arrays FET, with optimal performances in a physiological concentration range between 60 ng/mL and 100 μg/mL. We introduced a reference subtracted method to ensure a specific protein detection, and

reduce any common mode drift. We developed a pseudo-super-Nernstian sensor, which provides a 50-fold signal amplification in the case of pH sensing. We also demonstrated the detection of CRP in the whole concentration range of human biofluids, without the necessity of sample dilutions, making our platform an optimal candidate for the integration on wearable systems. In addition, the use of antibodies fragments immobilized on the sensor HfO_2 surface allows a specific label-free detection that overcomes the Debye screening. In terms of performance, the sensor showed a great stability over time (<20 pA/dec), low hysteresis in the double-sweep transfer characteristics, both in TG and in back-gate operation modes, and high versatility, thanks to the double-gate structure. High sensitivity, up to −1.2 nA/dec while operating the sensor in back-gate configuration, and a demonstrated stability in buffer make the proposed system a promising candidate for an industrial integration on a CMOS wearable multimarker sensing platform, offering the real-time diagnosis of acute or chronic inflammatory conditions.

REFERENCES

[1] M. Sharifpour *et al.*, "C-reactive protein as a prognostic indicator in hospitalized patients with COVID-19," *PLoS ONE*, vol. 15, no. 11, Nov. 2020, Art. no. e0242400, doi: 10.1371/journal.pone.0242400.

[2] J.-R. Lavillegrand *et al.*, "Elevated plasma IL-6 and CRP levels are associated with adverse clinical outcomes and death in critically ill SARS-CoV-2 patients: Inflammatory response of SARS-CoV-2 patients," *Ann. Intensive Care*, vol. 11, no. 1, pp. 1–10, Jan. 2021, doi: 10.1186/s13613-020-00798-x.

[3] N. Ali, "Elevated level of C-reactive protein may be an early marker to predict risk for severity of COVID-19," *J. Med. Virol.*, vol. 92, no. 11, pp. 2409–2411, Nov. 2020, doi: 10.1002/jmv.26097.

[4] *Biosensing Based on Field-Effect Transistors (FET): Recent Progress and Challenges Elsevier Enhanced Reader*. Accessed: Nov. 17, 2021. [Online]. Available: https://reader.elsevier.com/reader/sd/pii/S016599362030296X?token=8F8B45714D60B8D9549663884CDD4A3D1D0C28845C588C413115A2B5B82C09E8A59F078CDB427AE250A04EB0AC1DC1AF&originRegion=eu-west-1&originCreation=20211117140150

[5] S. Ahoulou, E. Perret, and J.-M. Nedelec, "Functionalization and characterization of silicon nanowires for sensing applications: A review," *Nanomaterials*, vol. 11, no. 4, p. 999, Apr. 2021, doi: 10.3390/nano11040999.

[6] J. H. Chua, R.-E. Chee, A. Agarwal, S. M. Wong, and G.-J. Zhang, "Label-free electrical detection of cardiac biomarker with complementary metal-oxide semiconductor-compatible silicon nanowire sensor arrays," *Anal. Chem.*, vol. 81, no. 15, pp. 6266–6271, Aug. 2009, doi: 10.1021/ac901157x.

[7] R. Elnathan *et al.*, "Biorecognition layer engineering: Overcoming screening limitations of nanowire-based FET devices," *Nano Lett.*, vol. 12, no. 10, pp. 5245–5254, Oct. 2012, doi: 10.1021/nl302434w.

[8] I. Lee, X. Luo, J. Huang, X. T. Cui, and M. Yun, "Detection of cardiac biomarkers using single polyaniline nanowire-based conductometric biosensors," *Biosensors*, vol. 2, no. 2, pp. 205–220, May 2012, doi: 10.3390/bios2020205.

[9] Y. Kutovyi *et al.*, "Highly sensitive and fast detection of C-reactive protein and troponin biomarkers using liquid-gated single silicon nanowire biosensors," *MRS Adv.*, vol. 5, no. 16, pp. 835–846, Mar. 2020, doi: 10.1557/adv.2020.60.

[10] M. A. M. Azmi *et al.*, "Highly sensitive covalently functionalised integrated silicon nanowire biosensor devices for detection of cancer risk biomarker," *Biosensors Bioelectron.*, vol. 52, pp. 216–224, Feb. 2014, doi: 10.1016/j.bios.2013.08.030.

[11] G. Zheng, F. Patolsky, Y. Cui, W. U. Wang, and C. M. Lieber, "Multiplexed electrical detection of cancer markers with nanowire sensor arrays," *Nature Biotechnol.*, vol. 23, pp. 1294–1301, Sep. 2005, doi: 10.1038/nbt1138.

[12] F. Patolsky, G. Zheng, and C. M. Lieber, "Fabrication of silicon nanowire devices for ultrasensitive, label-free, real-time detection of biological and chemical species," *Nature Protocols*, vol. 1, no. 4, pp. 1711–1724, Nov. 2006, doi: 10.1038/nprot.2006.227.

[13] G.-J. Zhang, Z. H. H. Luo, M. J. Huang, G. K. I. Tay, and E.-J.-A. Lim, "Morpholino-functionalized silicon nanowire biosensor for sequence-specific label-free detection of DNA," *Biosensors Bioelectron.*, vol. 25, no. 11, pp. 2447–2453, Jul. 2010, doi: 10.1016/j.bios.2010.04.001.

[14] G.-J. Zhang *et al.*, "Silicon nanowire biosensor for highly sensitive and rapid detection of Dengue virus," *Sens. Actuators B, Chem.*, vol. 146, no. 1, pp. 138–144, Apr. 2010, doi: 10.1016/j.snb.2010.02.021.

[15] S. Klinghammer *et al.*, "Nanosensor-based real-time monitoring of stress biomarkers in human saliva using a portable measurement system," *ACS Sensors*, vol. 5, no. 12, pp. 4081–4091, Dec. 2020, doi: 10.1021/acssensors.0c02267.

[16] F. Puppo *et al.*, "Femto-molar sensitive field effect transistor biosensors based on silicon nanowires and antibodies," in *Proc. IEEE Sensors*, Nov. 2013, pp. 1–4, doi: 10.1109/ICSENS.2013.6688205.

[17] G.-J. Zhang, J. H. Chua, R.-E. Chee, A. Agarwal, and S. M. Wong, "Label-free direct detection of MiRNAs with silicon nanowire biosensors," *Biosensors Bioelectron.*, vol. 24, no. 8, pp. 2504–2508, Apr. 2009, doi: 10.1016/j.bios.2008.12.035.

[18] M.-H. Lee, K.-N. Lee, S.-W. Jung, W.-H. Kim, K.-S. Shin, and W.-K. Seong, "Quantitative measurements of C-reactive protein using silicon nanowire arrays," *Int. J. Nanomed.*, vol. 3, no. 1, pp. 117–124, Mar. 2008.

[19] S. Vitusevich, "Characteristic frequencies and times, signal-to-noise ratio and light illumination studies in nanowire FET biosensors : Invited paper," in *Proc. IEEE Ukrainian Microw. Week (UkrMW)*, Sep. 2020, pp. 580–585, doi: 10.1109/UkrMW49653.2020.9252698.

[20] L. Barboni, M. Siniscalchi, and B. Sensale, "TFET-based circuit design using the transconductance generation efficiency g_m/I_d method," *IEEE J. Electron Devices Soc.*, vol. 3, no. 3, pp. 208–216, May 2015, doi: 10.1109/JEDS.2015.2412118.

[21] L. Liu *et al.*, "Analog and RF analysis of gate all around silicon nanowire MOSFETs," in *Proc. Joint Int. EUROSOI Workshop Int. Conf. Ultimate Integr. Silicon (EUROSOI-ULIS)*, Apr. 2017, pp. 176–179, doi: 10.1109/ULIS.2017.7962575.

[22] G. Rosaz *et al.*, "High-performance silicon nanowire field-effect transistor with silicided contacts," *Semicond. Sci. Technol.*, vol. 26, no. 8, Aug. 2011, Art. no. 085020, doi: 10.1088/0268-1242/26/8/085020.

[23] A. Girardi and S. Bampi, "Power constrained design optimization of analog circuits based on physical gm/I_D characteristics," *J. Integr. Circuits Syst.*, vol. 2, no. 1, pp. 22–28, Sep. 2007.

[24] F. Silveira, D. Flandre, and P. Jespers, "A g_m/I_D based methodology for the design of CMOS analog circuits and its application to the synthesis of a silicon-on-insulator micropower OTA," *IEEE J. Solid-State Circuits*, vol. 31, no. 9, pp. 1314–1319, Oct. 1996, doi: 10.1109/4.535416.

[25] C. Enz, M.-A. Chalkiadaki, and A. Mangla, "Low-power analog/RF circuit design based on the inversion coefficient," in *Proc. 41st Eur. Solid-State Circuits Conf. (ESSCIRC)*, Sep. 2015, pp. 202–208, doi: 10.1109/ESSCIRC.2015.7313863.

[26] L. Capua, S. Sheibani, S. Kamaei, J. Zhang, and A. M. Ionescu, "Extended-gate FET cortisol sensor for stress disorders based on aptamers-decorated graphene electrode: Fabrication, experiments and unified analog predictive modeling," in *IEDM Tech. Dig.*, Dec. 2020, pp. 35.2.1–35.2.4, doi: 10.1109/IEDM13553.2020.9372063.

[27] S. Zafar, C. D'Emic, A. Afzali, B. Fletcher, Y. Zhu, and T. Ning, "Optimization of pH sensing using silicon nanowire field effect transistors with HfO_2 as the sensing surface," *Nanotechnology*, vol. 22, no. 40, Oct. 2011, Art. no. 405501, doi: 10.1088/0957-4484/22/40/405501.

[28] S. Rollo, D. Rani, W. Olthuis, and C. P. García, "High performance Fin-FET electrochemical sensor with high-k dielectric materials," *Sens. Actuators B, Chem.*, vol. 303, Jan. 2020, Art. no. 127215, doi: 10.1016/j.snb.2019.127215.

[29] J.-H. Ahn, B. Choi, and S.-J. Choi, "Understanding the signal amplification in dual-gate FET-based biosensors," *J. Appl. Phys.*, vol. 128, no. 18, Nov. 2020, Art. no. 184502, doi: 10.1063/5.0010136.

[30] L. M. Helleckes, M. Osthege, W. Wiechert, E. V. Lieres, and M. Oldiges, "Bayesian calibration, process modeling and uncertainty quantification in biotechnology," *bioRxiv*, Jun. 2021, doi: 10.1101/2021.06.30.450546.